Research Square

Preprints are preliminary reports that have not undergone peer review.
They should not be considered conclusive, used to inform clinical practice,
or referenced by the media as validated information.

Endothelial Shank3 deficiency in male mice is associated with non-fibrotic eccentric cardiac remodeling

Eunhee Chung

eunhee.chung@utsa.edu

University of Texas at San Antonio

Ayodeji Osidele

University of Texas at San Antonio

Yun-Ju Fang

University of Texas at San Antonio

Abigail Gomez

University of Texas at San Antonio

Courtney P. Cornitius

University of Texas at San Antonio

Soo-Chan Lee

Texas Tech University Health Sciences Center

Il Hwan Kim

University of Tennessee Health Science Center

Research Article

Keywords: Shank3, cardiac remodeling, endothelium, mitochondrial bioenergetics, cardiac gene expression

Posted Date: November 25th, 2026

DOI: https://doi.org/10.21203/rs.3.rs-11732875/v1

License: This work is licensed under a Creative Commons Attribution 4.0 International License.
Read Full License

Additional Declarations: No competing interests reported.

Endothelial *Shank3* deficiency in male mice is associated with non-fibrotic eccentric cardiac remodeling

Eunhee Chung[1*], Ayodeji Osidele[1], Yun-Ju Fang[1], Abigail Gomez[1], Courtney P. Cornitius[2,3], Soo-Chan Lee[4], Il Hwan Kim[5]

[1]Department of Kinesiology, University of Texas at San Antonio, San Antonio, TX, USA. [2]Department of Molecular Microbiology and Immunology, University of Texas at San Antonio, San Antonio, TX, USA. [3]Department of Biology, Northwest Vista College, San Antonio, TX, USA. [4]Department of Immunology and Molecular Microbiology, Texas Tech University Health Sciences Center, Lubbock, TX. USA. [5]Department of Anatomy and Neurobiology, University of Tennessee Health Science Center, Memphis, TN, USA.

***Corresponding author:** Eunhee Chung, Ph.D., One UTSA Circle, Department of Kinesiology, University of Texas at San Antonio, San Antonio, TX 78249, USA

Tel.: +1 210-458-6023; Fax: + 1 210-458-5873. eunhee.chung@utsa.edu

Eunhee Chung: https://orcid.org/0000-0002-4501-9333
Ayodeji Osidele: https://orcid.org/0009-0006-7073-1492
Yun-Ju Fang: https://orcid.org/0009-0004-6944-2322
Abigail Gomez: https://orcid.org/0009-0009-4903-5494
Courtney P Cornitius: https://orcid.org/0000-0002-9962-9452
Soo-Chan Lee: https://orcid.org/0000-0002-7792-5947
Il Hwan Kim: https://orcid.org/0000-0002-8429-1030

Abstract

SHANK3 is an autism spectrum disorder risk gene that, in the human heart, is expressed mainly in endothelial cells, but its role in the heart outside cardiomyocytes is unknown. In mice, endothelial *Shank3* deletion (*Shank3*$^{f/f;}$Tek-Cre) produces male-specific neurovascular and behavioral phenotypes; whether the heart is similarly affected has not been examined. We therefore followed adult male knockout (KO) mice and age-matched C57BL/6J wild-type (WT) mice from 12 to 21 wk of age. At 12–16 wk, KO mice had higher baseline aortic peak velocity, and isovolumic relaxation time shortened during dobutamine only in KO mice. At 20–21 wk, despite lower body weight, KO mice had greater left ventricular (LV) and atrial weights, larger LV internal diameters with unchanged wall thickness, and lower ejection fraction, fractional shortening, and posterior wall thickening, whereas stroke volume and cardiac output were preserved. This eccentric remodeling occurred without detectable interstitial fibrosis or increases in *Nppa*, *Acta1*, or *Myh7* mRNA. *Myh6* and *Nppb* mRNA were lower, whereas *Ppargc1a* mRNA and the phospho-AMPK/AMPK ratio were higher. Carbohydrate- and fatty acid-supported respiration and H_2O_2 emission of isolated cardiac mitochondria were preserved, and mitochondrial 4-HNE-modified protein was lower. These findings show that *Shank3* deletion in Tek-Cre–targeted cells is associated with eccentric LV remodeling and mildly reduced systolic function, without detectable increases in myocardial fibrosis or impairment of mitochondrial respiratory capacity. Our findings suggest that endothelial *Shank3* may also contribute to the maintenance of cardiac structure and function.

Keywords: *Shank3*, cardiac remodeling, endothelium, mitochondrial bioenergetics, cardiac gene expression

Introduction

Autism spectrum disorder (ASD) is often accompanied by medical conditions outside the nervous system, but the cardiovascular effects of ASD-associated genes are not well defined [2]. *SHANK3* (SH3 and multiple ankyrin repeat domains 3) encodes a scaffolding protein best known for organizing the postsynaptic density of excitatory synapses. Deletions at chromosome 22q13.3 or pathogenic variants in *SHANK3* cause Phelan-McDermid syndrome (PMS), and loss of *SHANK3* is considered the main cause of its neurological features [33]. *SHANK3* mRNA is also abundant in the heart [41]. In human cardiac single-cell data summarized by Kim et al., it is detected mainly in endothelial cells, followed by cardiomyocytes, smooth muscle cells, and fibroblasts [19]. Cardiac SHANK3 protein, however, has not been consistently detected. Clinical cardiac data are still limited. In a recent series of five patients with pathogenic *SHANK3* variants, all had cardiac involvement, and three had mild or borderline ventricular dysfunction [10]. In mice, global *Shank3* Δexon 4–9 mutants showed small differences from wild-type mice, including increased left ventricular (LV) anterior and posterior wall thickness, rather than the eccentric dilation examined here [2].

Most mechanistic studies of cardiac *Shank3* have focused on cardiomyocytes. *Shank3* forms a complex with phospholipase Cβ1b at the cardiac sarcolemma, and knockdown of *Shank3* reduces Gq-mediated hypertrophic signaling in neonatal rat cardiomyocytes [15]. In vivo, the effects of altering *Shank3* levels appear to depend on the context. *Shank3* knockout worsened cardiac dysfunction after myocardial infarction, whereas *Shank3* overexpression reduced it [25]. In contrast, inducible cardiomyocyte-specific deletion of *Shank3* enhanced mitophagy and preserved cardiac function in aged mice [43], and modest overexpression of *Shank3* caused arrhythmias, sudden cardiac death, and impaired calcium handling [22]. These studies suggest that cardiac function is sensitive to *Shank3* levels. The effect of deleting *Shank3* in non-myocyte cells has not been tested directly.

Endothelial cells are among the most abundant cells in the heart [30]. The cardiac endothelium regulates myocardial growth, contractility, and rhythm through paracrine signals such as nitric oxide, endothelin-1, and neuregulin-1 [5]. Kim et al. recently showed that *SHANK3* is expressed in brain endothelial cells, where it maintains tight junctions through β-catenin signaling [20]. Endothelial *Shank3* knockout (eShank3-KO) mice showed male-specific blood–brain barrier hyperpermeability as neonates. Although barrier function recovered in adulthood, adult male mice still had reduced neuronal excitability and impaired social behavior [20]. These findings show that loss of endothelial *Shank3* can have lasting effects beyond the vasculature. Whether it also affects the structure, function, or metabolism of the adult heart is unknown.

Pathological cardiac remodeling is often accompanied by reactivation of a fetal gene program, interstitial fibrosis, and impaired mitochondrial function [8,45]. The aim of this study was therefore to characterize the cardiac phenotype of adult male eShank3-KO mice. We hypothesized that loss of endothelial *Shank3* would alter LV structure and function and that these changes would be accompanied by changes in myocardial gene expression, fibrosis, and mitochondrial function.

Materials and methods

Animals

Breeding mice were generously provided by Dr. Il Hwan Kim (University of Tennessee Health Science Center, Memphis, TN, USA), as described previously [20], and were maintained and bred at the University of Texas at San Antonio. Mice carrying a *Shank3* allele with loxP sites flanking exons 4–9 (*Shank3*$^{f/f}$) [42] and Tek-Cre transgenic mice (B6.Cg-Tg(Tek-cre)1Ywa/J; The Jackson Laboratory, stock #008863) [21] were used. To generate mice heterozygous for the floxed *Shank3* allele and carrying Tek-Cre (*Shank3*$^{f/+}$;Tek-Cre), male Tek-Cre mice were crossed with female mice homozygous for the floxed *Shank3* allele. Male *Shank3*$^{f/+}$;Tek-Cre offspring were subsequently crossed with *Shank3*$^{f/f}$ females to generate *Shank3*$^{f/+}$;Tek-Cre and

Shank3$^{f/f;}$Tek-Cre offspring. Male *Shank3*$^{f/f;}$Tek-Cre mice were used as endothelial Shank3-knockout (eShank3-KO) mice. Age-matched male C57BL/6J mice (The Jackson Laboratory, stock #000664) were used as wild-type (WT) controls, as both parental lines had been backcrossed onto the C57BL/6J background for six generations [20]. Although the breeding strategy could generate Cre-negative floxed littermates (*Shank3*$^{f/+}$ and *Shank3*$^{f/f}$ without Cre), these mice were not included as controls because breeding efforts and animal allocation were prioritized toward generating enough eShank3-KO mice for the planned experiments. Tek-Cre-only controls were also not included. WT mice were purchased at 10 wk of age and acclimated for at least 2 wk in the same animal facility before the first measurement. All mice were housed under controlled conditions (22 ± 1°C, 40–60% humidity, 12:12-h light-dark cycle) with ad libitum access to water and standard chow (PicoLab Select Rodent 50 IF/6F, 5V5R; LabDiet) [11]. Genotypes were determined by PCR analysis of ear-punch samples collected from weaned pups using the primers listed in **Supplementary Table 1** and were reconfirmed by PCR analysis of tail DNA following completion of physiological measurements. Only male mice were studied because autism spectrum disorder (ASD) is more prevalent in males than in females [37] and because eShank3-KO mice exhibit male-predominant phenotypes [20].

Supplementary Table 1. Shank3 genotyping primers.

Primer	5′–3′ sequence	Orientation	Amplicon size	Remarks
SL814	AACAGGACCCCAATATGTCAA G	Forward	479 bp	SH-AFLP-F
SL815	GGCTATGTTCATGGGATCTTGT	Reverse	479 bp	SH-AFLP-R

Primer	5′−3′ sequence	Orientation	Amplicon size	Remarks
SL816	AGGACAGGTGACAGTCAATGG	Forward	660 or 317 bp	Shank3 (e4-9) f/f primer: sh3preLoxP1-F
SL817	GCCTTGTCTGGTGGTACAGG	Reverse	660 or 317 bp	Shank3 (e4-9) f/f primer: sh3preLoxP1-R
SL818	GGCTATGTTCATGGGATCTTGT	Reverse	660 or 317 bp	Knock-out: sh3preLoxP1-R
SL820	GCGGTCTGGCAGTAAAAACTATC	Forward	102 bp	CMV Cre-Tg-F
SL821	GTGAAACAGCATTGCTGTCACTT	Reverse	102 bp	CMV Cre-Tg-R
SL822	CTAGGCCACAGAATTGAAAGATCT	Forward	324 bp	CMV Cre-IPC-F
SL823	GTAGGTGGAAATTCTAGCATCATCC	Reverse	324 bp	CMV Cre-IPC-R

Mice were genotyped by polymerase chain reaction (PCR) using the listed primers above. Primers SL814 and SL815 screen for the expression of Shank3. Primers SL816, SL817, and SL818 screen for whether one or both alleles of Shank3 are floxed; if one allele is floxed then the expected band sizes would be 660 base pairs (bp) and 317 bp but if both alleles are floxed, then the expected band size would be 317 bp upon visual confirmation on gel electrophoresis. Primers SL820 and SL821 screen for the presence of Cre recombinase. Primers SL822 and SL823 are for the internal positive control (IPC).

Experimental design

Age-matched groups of WT and eShank3-KO mice were evaluated at different ages between 12 and 21 weeks. Mitral inflow was assessed at 12–15 weeks, and aortic outflow was assessed at 16 weeks, both at baseline and during dobutamine stimulation. Doppler, echocardiographic, and histological analyses were performed by investigators blinded to genotype. No prior power calculation was performed. Exact numbers of independent animals are reported in the corresponding figure legends.

Doppler flow velocity measurements

Cardiac function was assessed using a Doppler Flow Velocity System (DFVS; Scintica, Webster, TX, USA), as previously described [31,29]. Mice were anesthetized with isoflurane (5% induction; 1.0–1.5% maintenance) in 100% oxygen, and body temperature was maintained at 37°C. Doppler signals were acquired using a 10-MHz probe with simultaneous Lead II ECG recording. Measurements were obtained at baseline and 3–5 min after dobutamine administration (1.5 µg/g, intraperitoneal [i.p.]) [11]. If heart rate did not increase, the dobutamine assessment was discontinued, and only baseline data were retained.

Mitral inflow measurements included peak E- and A-wave velocities, E/A ratio, isovolumic relaxation time (IVRT), and isovolumic contraction time (IVCT). Because mitral and aortic flows were recorded separately, IVRT and IVCT were calculated from ECG R-wave–referenced event times using cardiac cycles with comparable R–R intervals [29]. Aortic outflow measurements included peak velocity, ejection time, and mean acceleration. For each measurement, 2–4 cardiac cycles were averaged and analyzed offline using Doppler Signal Processing Workstation software (Scintica, Webster, TX, USA). Recordings with unstable Doppler signals were excluded.

Echocardiography

Cardiac structure and LV systolic function were assessed by M-mode echocardiography in the mid-papillary short-axis view using a NEXTGen LOGIQ e R7 ultrasound system (GE) with a 10–22 MHz transducer, as previously described [14]. Mice were anesthetized with isoflurane (5% for induction and 1.5% for maintenance) and placed supine on a warming pad. All measurements were averaged over three consecutive cardiac cycles. Wall thickening (%PWT and %AWT) was calculated as (systolic − diastolic wall thickness)/diastolic wall thickness × 100.

Body composition

Fat mass, lean mass, and free body fluid (FBF) were measured in conscious mice using a time-domain nuclear magnetic resonance (TD-NMR) analyzer (minispec LF50, Bruker, The Woodlands, TX, USA) [16] in a subset of mice (WT, n=11; KO, n = 10). Each mouse was weighed and placed in a restraining tube without anesthesia, and measurements were completed within approximately 2 min. Body composition was assessed 3–5 days before tissue collection, approximately 3–4 h after the onset of the light phase, under ad libitum-fed conditions. Fat mass, lean mass, and FBF were expressed in grams and as percentages of body weight (BW).

Tissue collection and morphometry

At 20–21 wk of age, mice were euthanized by isoflurane inhalation in an induction chamber followed by cervical dislocation. Hearts were rapidly excised and rinsed in cold phosphate-buffered saline (PBS). The atria were removed and weighed, and the LV (including the septum) was dissected and weighed. Tibia length was measured. Approximately 30 mg of fresh LV tissue was used to isolate mitochondria by differential centrifugation for same-day respirometry [14]. The mid-papillary region was fixed in 1X Z-Fix for histology (n=3/group), and the remaining LV was frozen in liquid nitrogen and stored at −80°C for RNA and protein analyses.

Cardiac mitochondrial respiration and H_2O_2 production

Mitochondria were isolated from approximately 30 mg of fresh LV tissue by differential centrifugation [14]. Oxygen consumption and H_2O_2 emission were measured simultaneously at 37°C in MiR05 using an O2k-FluoRespirometer (Oroboros Instruments, Innsbruck, Austria) with the Amplex UltraRed detection system, as previously described [23,11]. Carbohydrate-supported respiration was assessed with malate (1 mM) and pyruvate (5 mM; PM_{LEAK}), followed by ADP (2.5 mM; PM_P), glutamate (10 mM), and succinate (20 mM; $CI+CII_P$). For fatty acid-supported respiration, malate (1 mM) and octanoylcarnitine (0.5 mM) were used to assess LEAK respiration (FAO_{LEAK}), followed sequentially by ADP (2.5 mM; FAO_P), pyruvate (5 mM; FAO_PCI_P), glutamate (10 mM), and succinate (20 mM; FAO_P $CI+CII_P$). Coupling efficiency was calculated as (P − L)/P, where P and L are OXPHOS and LEAK respiration, respectively. H_2O_2 emission was measured with pyruvate and malate in the LEAK and OXPHOS states and expressed as an absolute rate (JH_2O_2) and relative to O_2 flux (JH_2O_2/JO_2). Respiration rates were normalized to mitochondrial protein measured with a BCA assay (#23227; Thermo Fisher Scientific, Waltham, MA). Preparations with unstable oxygen signals, chamber artifacts, or no ADP-stimulated respiration were excluded as technical failures [11].

mRNA analysis

A targeted panel of 17 transcripts was selected a priori to represent fibrosis, hypertrophy and heart failure, and angiogenesis. Left ventricular RNA was isolated with Tri Reagent (Molecular Research Center, Cincinnati, OH) according to the manufacturer's instructions. RNA concentration and purity were assessed by spectrophotometry (A_{260}/A_{280}), and 2 µg of RNA was reverse transcribed using iScript Reverse Transcription Supermix (Bio-Rad, Hercules, CA, USA), followed by quantitative real-time PCR with SYBR Green chemistry on a Bio-Rad CFX system. Samples were run in duplicate, and primer sequences and validation have been reported previously [11,6]. Ct values were normalized to ribosomal protein lateral stalk subunit

P0 (36B4; forward, 5′-CTGTGCCAGCTCAGAACACTG-3′; reverse, 5′-TGATCAGCCCGAAGGAGAAG-3′). 36B4 Ct values did not differ between genotypes. Relative mRNA expression was calculated using the $2^{-\Delta\Delta Ct}$ method and is presented as fold change relative to the WT group.

Western Blot Analysis

Western blotting was performed as previously described [11]. Freshly isolated mitochondria remaining after respirometry were snap-frozen and stored at −80°C. LV tissue was homogenized in RIPA buffer (50 mM Tris-HCl, pH 7.6, 150 mM NaCl, 1% NP-40, 0.5% sodium deoxycholate, and 0.1% SDS; Item No. 10010263, Cayman Chemical, Ann Arbor, MI, USA) containing protease and phosphatase inhibitors (PI78443, Thermo Fisher Scientific, Waltham, MA, USA). Equal amounts of protein (30 µg) were separated by SDS-PAGE and transferred to PVDF membranes. Following transfer, PVDF membranes were stained with Ponceau S to assess protein loading and transfer uniformity. Membranes were then horizontally sectioned according to the expected molecular weights of the target proteins. Individual membrane sections were probed separately with the corresponding primary antibodies to avoid repeated stripping and reprobing. Mitochondrial fractions were probed for OXPHOS complexes I–V (ab110413, 1:1,000, Abcam, Waltham, MA, USA) and 4-HNE-modified proteins (ab48506, 1:1,000, Abcam, Waltham, MA, USA), with VDAC1 (ab14734, 1:1,000, Abcam, Waltham, MA, USA) as the loading control. LV homogenates were probed for nitrotyrosine (sc-32757, 1:1,000, Santa Cruz Biotechnology, Dallas, TX, USA), p-AMPK (Thr172; #2535, [1:1,000], Cell Signaling Technology, Danvers, MA, USA), and total AMPK (#2532, [1:1,000], Cell Signaling Technology, Danvers, MA, USA), with vinculin (D16H11, 1:5,000, Cell Signaling Technology, Danvers, MA, USA) as the loading control. Bands were quantified by densitometry (Image Lab, Bio-Rad, Hercules, CA, USA), and normalized to the loading control. To account for variation between

blots, values were expressed relative to the mean of WT samples on the same blot, and values from samples run on multiple blots were averaged to obtain one value per mouse.

Histological Analysis

Heart tissue from the mid-papillary region was immersion-fixed in Z-Fix solution (Anatech Ltd., Battle Creek, MI, USA), paraffin-embedded, and sectioned at 5 μm. Sections were stained with Masson's trichrome (#9179B, Newcomer Supply, Waunakee, WI, USA) and Weigert's iron hematoxylin (ab245882, Abcam, Waltham, MA, USA) to assess myocardial fibrosis. Collagen-positive area was quantified using Fibrosoft, as previously described [32]. For each mouse (n = 3 per genotype), three sections were analyzed. The entire myocardial cross-sectional area was imaged at 20× magnification using an Olympus DP73 camera and cellSens Standard software (version 4.1; Olympus, Waltham, MA, USA). The number of imaging fields varied with section size (16–27 fields per section). Collagen-positive area, including perivascular regions, was expressed as a percentage of total myocardial tissue area for each section. The three section-level values were averaged to obtain one value per mouse, which served as the independent experimental unit for statistical analysis to avoid pseudo-replication [9].

Statistical Analysis

Data are presented as means ± SD, and exact P and q values are reported. Analyses were performed with GraphPad Prism 11 (GraphPad Software, LLC, San Diego, CA, USA). The mouse was the experimental unit, and technical replicates were averaged before analysis. Normality was assessed with the Shapiro–Wilk test. Two-group comparisons were made with unpaired, two-tailed Welch's t tests. Variables measured at baseline and during dobutamine were analyzed with mixed-effects models (restricted maximum likelihood) with genotype, dobutamine, and their interaction as fixed effects and mouse as a random effect, followed by uncorrected Fisher's least significant difference tests for pairwise comparisons. qRT-PCR gene groups, body composition variables, and OXPHOS complexes I–V were compared with multiple

Mann–Whitney tests, with the false discovery rate controlled within each family at Q = 5% using the two-stage step-up method [3]. Significance was set at $P < 0.05$ ($q < 0.05$ for FDR-controlled comparisons).

Results

Endothelial Shank3-KO mice have lower body weight and greater left ventricular and atrial weights.

To characterize the general phenotype of mice with endothelial *Shank3* deletion, we measured body weight (BW), body composition, and cardiac chamber weights in 20- to 21-wk-old wild-type (WT) and endothelial *Shank3*-knockout (KO) mice (WT, n = 16-18; KO, n =14-16). BW was lower in KO mice than in WT mice ($P = 0.0067$; Fig. 1a). Body composition was measured in a subset of mice (n = 10–11/group). Absolute fat mass, lean mass, and free body fluid (FBF)

Fig. 1

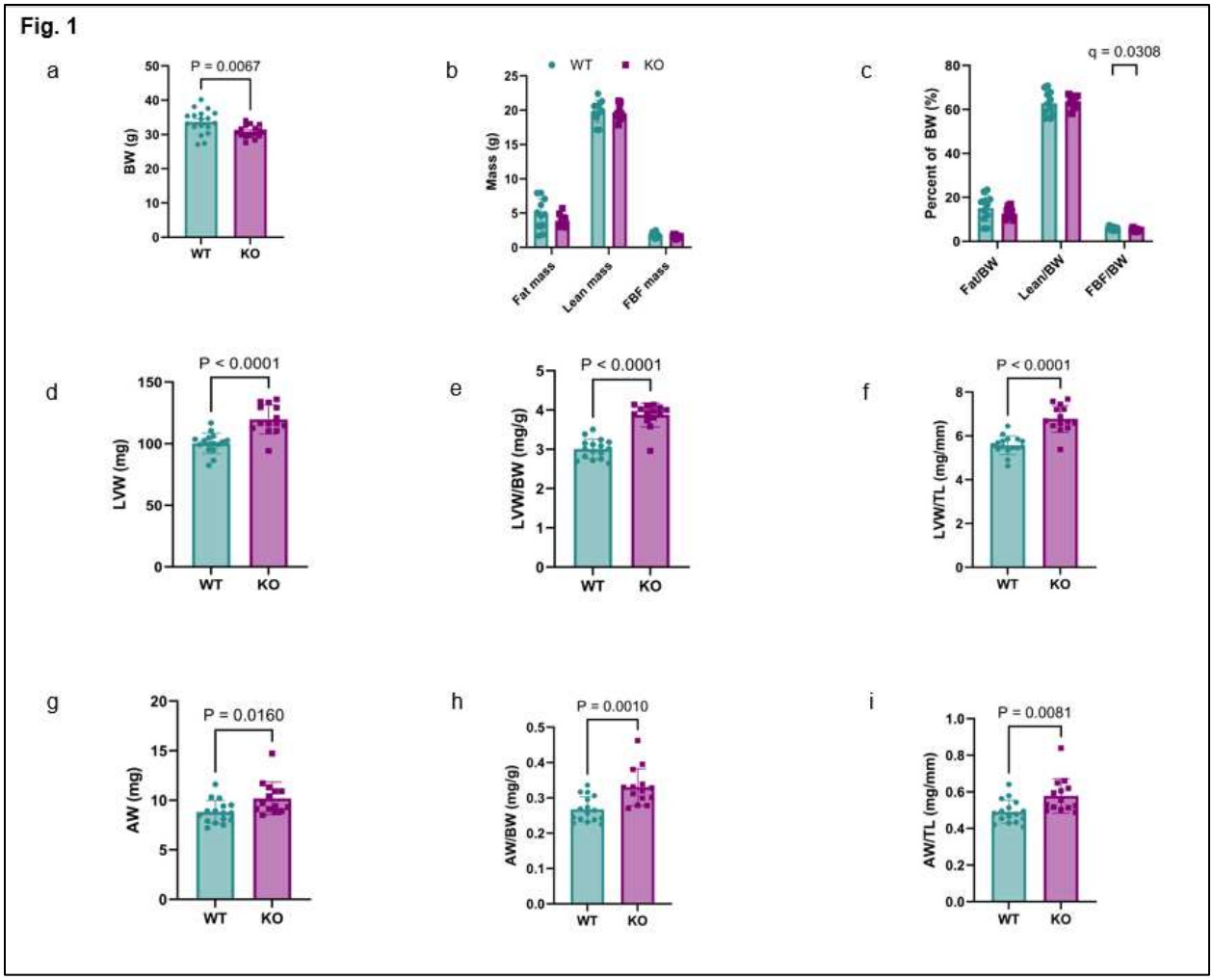

mass did not differ between groups (Fig. 1b). When expressed as a percentage of BW, fat mass (WT, 15.1 ± 6.1%; KO, 12.6 ± 2.6%) and lean mass (WT, 62.8 ± 5.5%; KO, 63.8 ± 2.9%) were also similar between groups, whereas FBF was lower in KO mice (WT, 6.1 ± 0.8%; KO, 5.2 ± 0.6%; q = 0.0308; Fig. 1c). Because all subsequent molecular and mitochondrial analyses were performed in left ventricular (LV) tissue, we used LV weight (LVW) as the primary index of cardiac mass. Despite their lower BW, KO mice had a greater LVW than WT mice (WT, 100.3 ± 8.26 mg; KO, 119.7 ± 11.71 mg; P < 0.0001; Fig. 1d). LVW remained greater in KO mice after normalization to BW (LVW/BW; P < 0.0001; Fig. 1e) and to tibia length (LVW/TL; P < 0.0001; Fig. 1f). Because BW was lower in KO mice, LVW/BW alone may overestimate the difference between groups. However, absolute LVW and LVW/TL were also greater in KO mice, indicating that the greater LVW was not explained by the difference in body size. Atrial weight (AW) was also greater in KO mice, both in absolute terms (P = 0.0160; Fig. 1g) and after normalization to BW (AW/BW; P = 0.0010; Fig. 1h) and to TL (AW/TL; P = 0.0081; Fig. 1i).

Similar Baseline Mitral Inflow but Greater IVRT Shortening During β-Adrenergic Stimulation in Endothelial Shank3-KO Mice

To assess left ventricular (LV) diastolic function and the response to β-adrenergic stimulation, mitral inflow was recorded by pulsed-wave Doppler at baseline and during dobutamine stimulation in 12-to 15-week-old WT and endothelial Shank3-KO mice (Fig. 2). Dobutamine increased heart rate in both WT (P = 0.0015) and KO mice (P < 0.0001), and heart rate during dobutamine did not differ between genotypes (P = 0.8577). At baseline, post hoc comparisons showed no genotype differences in E-peak velocity, A-peak velocity, E/A ratio, IVCT, or IVRT. Dobutamine did not change E-peak velocity (main effect of dobutamine, P = 0.4601), A-peak velocity (P = 0.2292), or E/A ratio (P = 0.2670). A-peak velocity was lower in KO than in WT mice across both conditions (main effect of genotype, P = 0.0327), although the genotype difference was not significant at baseline (P = 0.0990) or during dobutamine (P = 0.0884). IVCT was shorter during dobutamine (main effect of dobutamine, P = 0.0021), with no main effect of

genotype (P = 0.9918) and no genotype × dobutamine interaction (P = 0.5094), indicating that dobutamine shortened IVCT similarly in WT and KO mice. For IVRT, there was a significant main effect of dobutamine (P = 0.0099) and a significant genotype × dobutamine interaction (P = 0.041). Dobutamine shortened IVRT in KO mice (baseline: 12.4 ± 3.7 ms, n = 16; dobutamine: 7.5 ± 3.4 ms, n = 8; P = 0.0014) but not in WT mice (P = 0.6135).

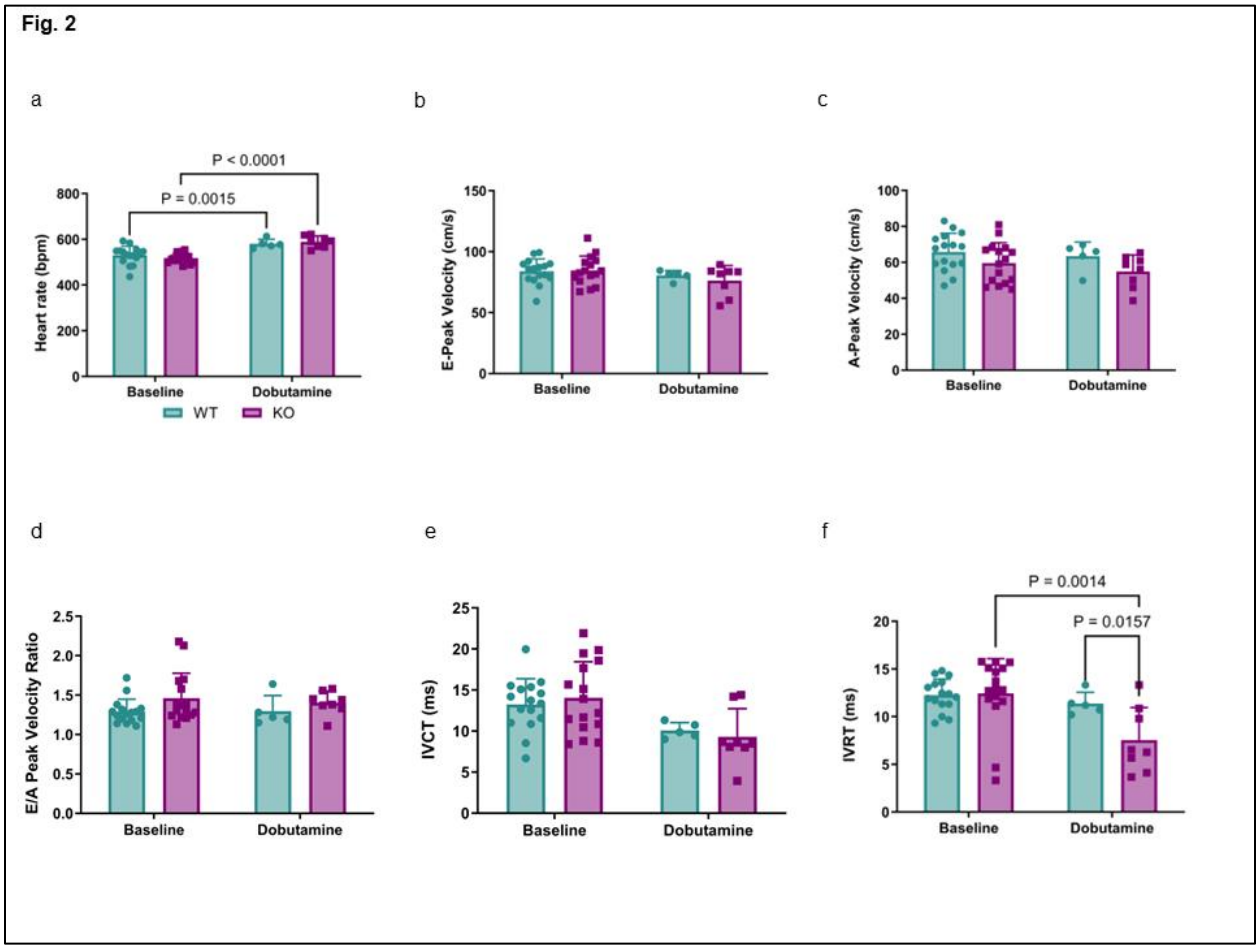

Higher Aortic Peak Velocity in Endothelial Shank3-KO Mice at Baseline and During β-Adrenergic Stimulation

To assess LV systolic function, aortic outflow was recorded by pulsed-wave Doppler at baseline and during dobutamine stimulation in 16-week-old WT and endothelial Shank3-KO mice (n = 12 WT and 13-16 KO; Fig. 3). Dobutamine increased heart rate in both WT (P < 0.0001) and KO mice (P = 0.0002), with no genotype × dobutamine interaction (P = 0.4005). During dobutamine,

heart rate was lower in KO than in WT mice (WT: 595.0 ± 13.3 bpm; KO: 571.6 ± 26.9 bpm; P = 0.0242). At baseline, aortic peak velocity was higher in KO than in WT mice (WT: 115.8 ± 11.3 cm/s; KO: 136.2 ± 18.4 cm/s; P = 0.0013), whereas mean acceleration (P = 0.263) and ejection time (P = 0.4178) did not differ between groups. In both groups (WT and KO), dobutamine increased peak velocity and mean acceleration and shortened ejection time (all P < 0.0001).

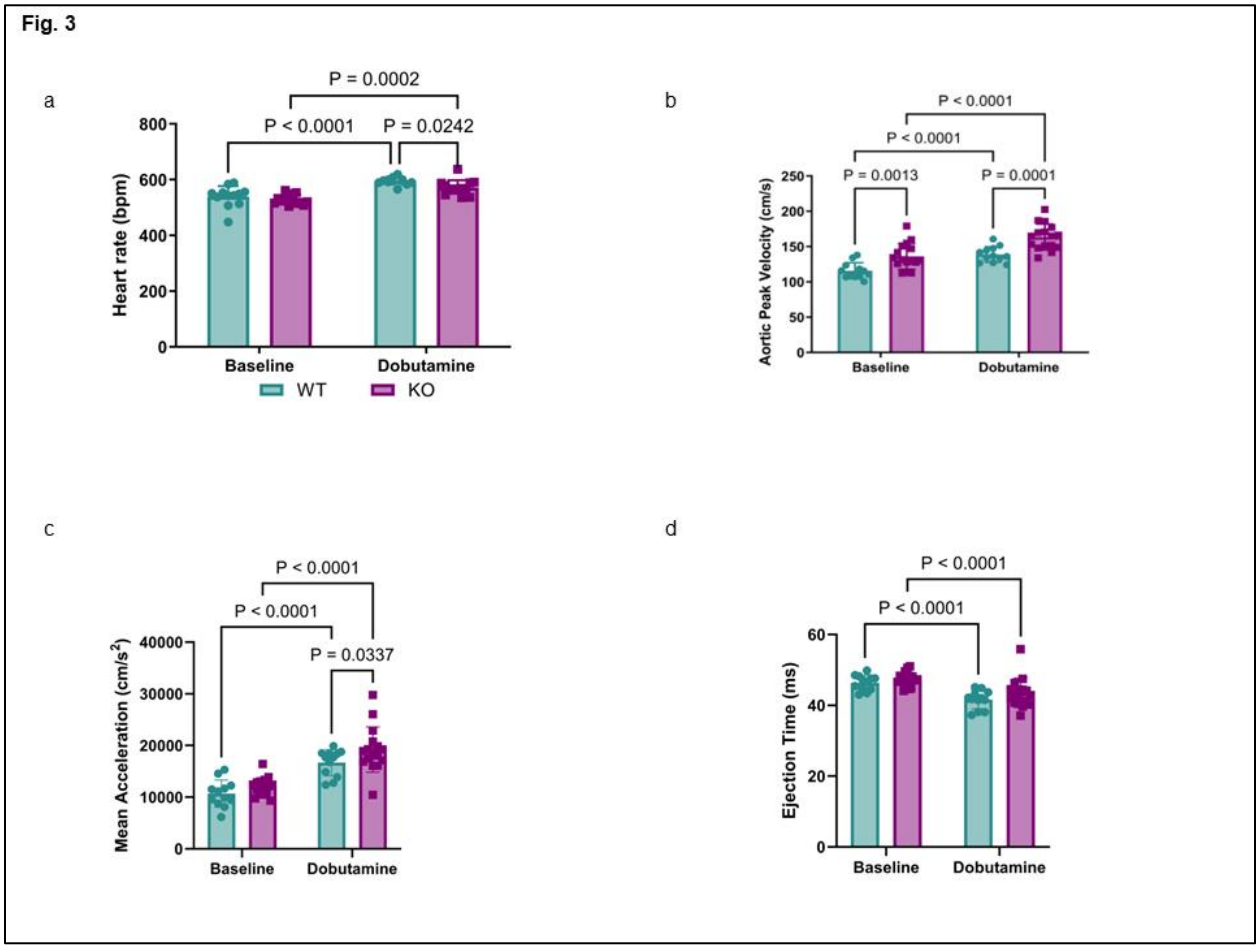

The genotype × dobutamine interaction was not significant for HR (P = 0.4005), peak velocity (P = 0.2771), mean acceleration (P = 0.4098), or ejection time (P = 0.3567), indicating that the dobutamine-induced change from baseline did not differ between genotypes. Because peak velocity was already higher in KO mice at baseline, it remained higher in KO than in WT mice during dobutamine (WT: 138.9 ± 10.9 cm/s; KO: 163.7 ± 18.3 cm/s; P = 0.0001). Mean

acceleration did not differ between groups at baseline but was higher in KO mice during dobutamine (P = 0.0337).

Endothelial Shank3 Deletion Is Associated With Left Ventricular Dilation and Reduced Systolic Function

To determine whether endothelial *Shank3* deletion affects LV structure and function at a later age, M-mode echocardiography was performed in the parasternal short-axis view at the mid-papillary level in 20- to 21-week-old WT and endothelial Shank3-KO mice (n = 15 WT and 15 KO; Fig. 4). Heart rate did not differ between genotypes (P = 0.1132; Fig. 4a). Anterior and posterior wall thicknesses in diastole and systole (LVAWd, LVAWs, LVPWd, and LVPWs) were also similar between genotypes (P = 0.2893, 0.9282, 0.6546, and 0.2214,

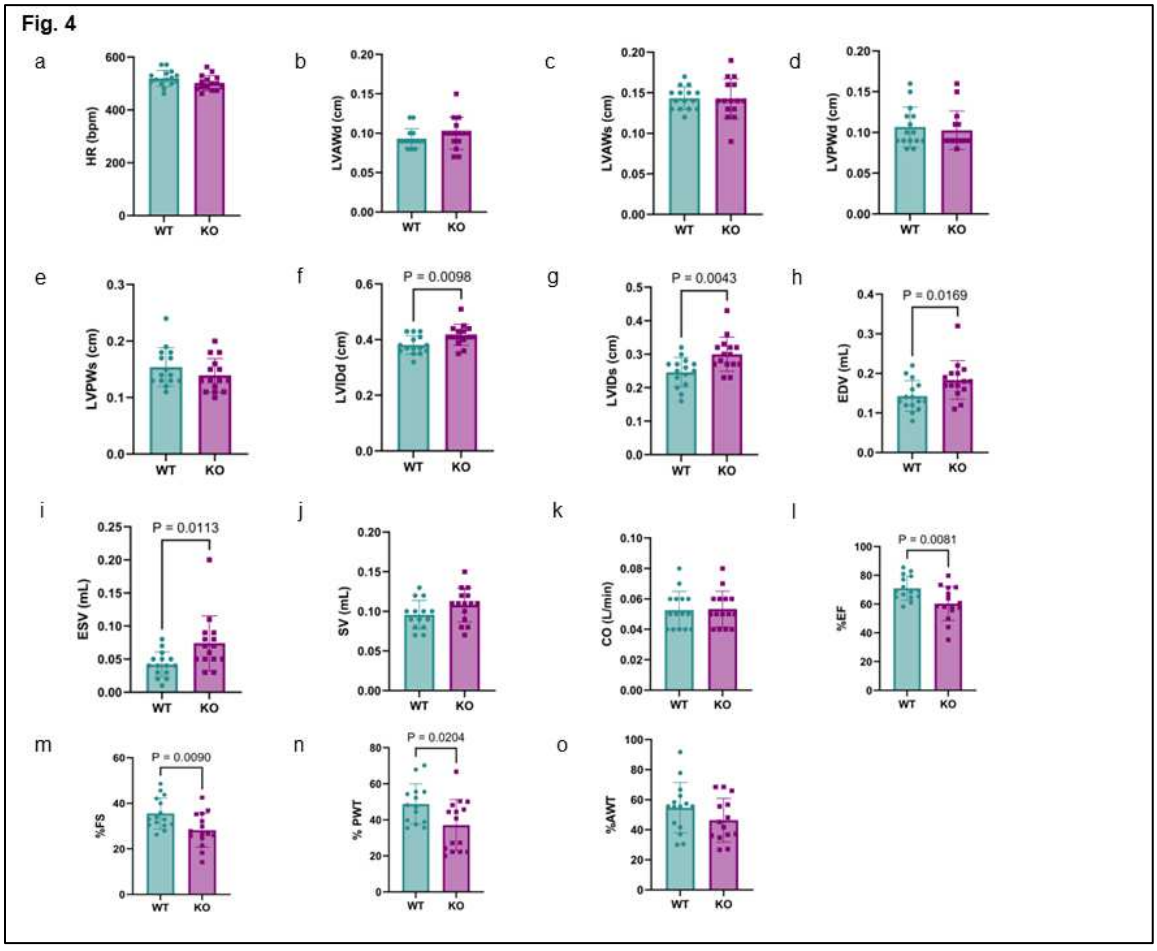

respectively; Fig. 4b–e). In contrast, LV internal diameter was larger in KO than in WT mice in

both diastole (LVIDd; P = 0.0098) and systole (LVIDs; P = 0.0043; Fig 4f, g). Consistent with these changes, end-diastolic volume (EDV; P = 0.0169) and end-systolic volume (ESV; P = 0.0113) were higher in KO mice (Fig. 4h, i), whereas stroke volume (SV; P = 0.1078) and cardiac output (CO; P = 0.8801) did not differ between genotypes (Fig. 4j, k). Ejection fraction (%EF; WT: 71.1 ± 8.3%; KO: 60.4 ± 11.7%; P = 0.0081), fractional shortening (%FS; P = 0.0090), and posterior wall thickening (%PWT; P = 0.0204) were lower in KO than in WT mice, whereas anterior wall thickening (%AWT) did not differ significantly (P = 0.163; Fig. 4l–o).

No Detectable Increase in Myocardial Collagen Deposition but Altered Myh6, Nppb, and Ppargc1a Expression in Endothelial Shank3-KO Hearts

Myocardial collagen-positive area did not differ between WT and endothelial *Shank3*-KO mice at 20–21 weeks of age (WT: 3.008 ± 0.236%; KO: 3.180 ± 1.392%; P = 0.8518; n = 3 per genotype; Fig. 5a, b). Similarly, mRNA expression of fibrosis-related genes (*Col1a1*, *Col3a1*, *Col8a1*, *Mmp3*, and *Ctgf*) did not differ between genotypes (Fig. 5c). We next measured the expression of genes associated with cardiac hypertrophy and heart failure. *Nppa*, *Acta1*, *Atp2a2*, and *Myh7* expression did not differ between genotypes (Fig. 5d). In contrast, expression of *Myh6*, which encodes α-myosin heavy chain, the predominant myosin heavy chain isoform in the adult mouse ventricle, was lower in KO than in WT mice (q = 0.0045). Expression of *Nppb*, which encodes B-type natriuretic peptide, was also lower in KO mice (q = 0.0045). Among angiogenesis-related genes, *Angpt1*, *Angpt2*, *Pdgfa*, *Vegfa*, and *Fgf2* did not differ between genotypes, whereas *Ppargc1a*, which encodes PGC-1α, a regulator of both mitochondrial metabolism and cardiac angiogenesis [26], was higher in KO mice (q = 0.0227;

Fig. 5e).

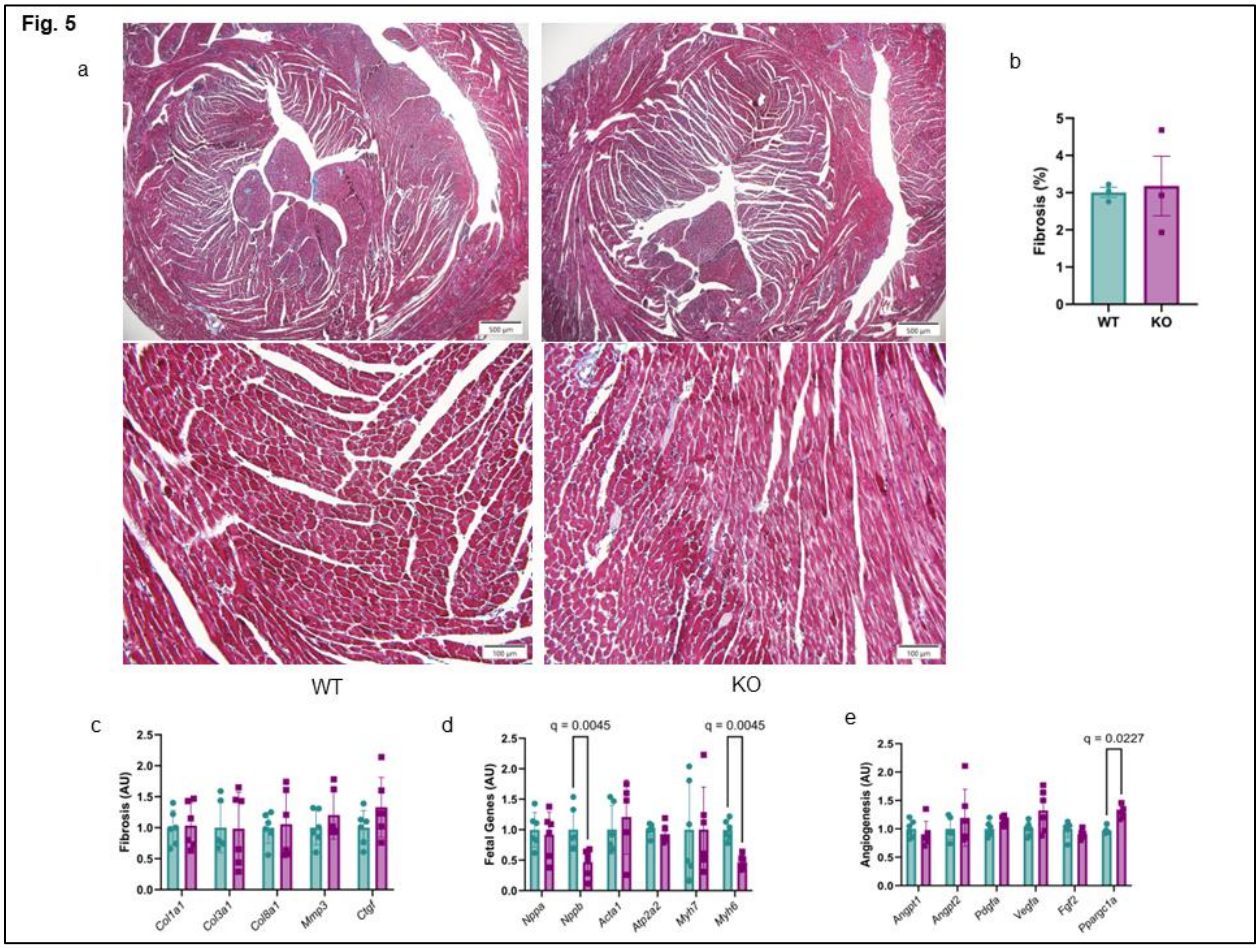

No Significant Genotype Differences in Cardiac Mitochondrial Respiration or H_2O_2 Emission were Detected

To determine whether LV dilation and reduced systolic function in endothelial Shank3-KO mice were associated with impaired cardiac mitochondrial function, mitochondrial respiration was measured by high-resolution respirometry in isolated mitochondria in 20-21-week-old WT and KO mice (n = 8 WT and 13 KO; Fig. 6a–d). With pyruvate and malate as substrates, LEAK respiration (PM_{LEAK}; P = 0.3221), ADP-stimulated OXPHOS (PMp; P = 0.0961), and maximal OXPHOS after the addition of glutamate and succinate (CI+CIIp; P = 0.4289) did not differ between genotypes (Fig. 6a–c).

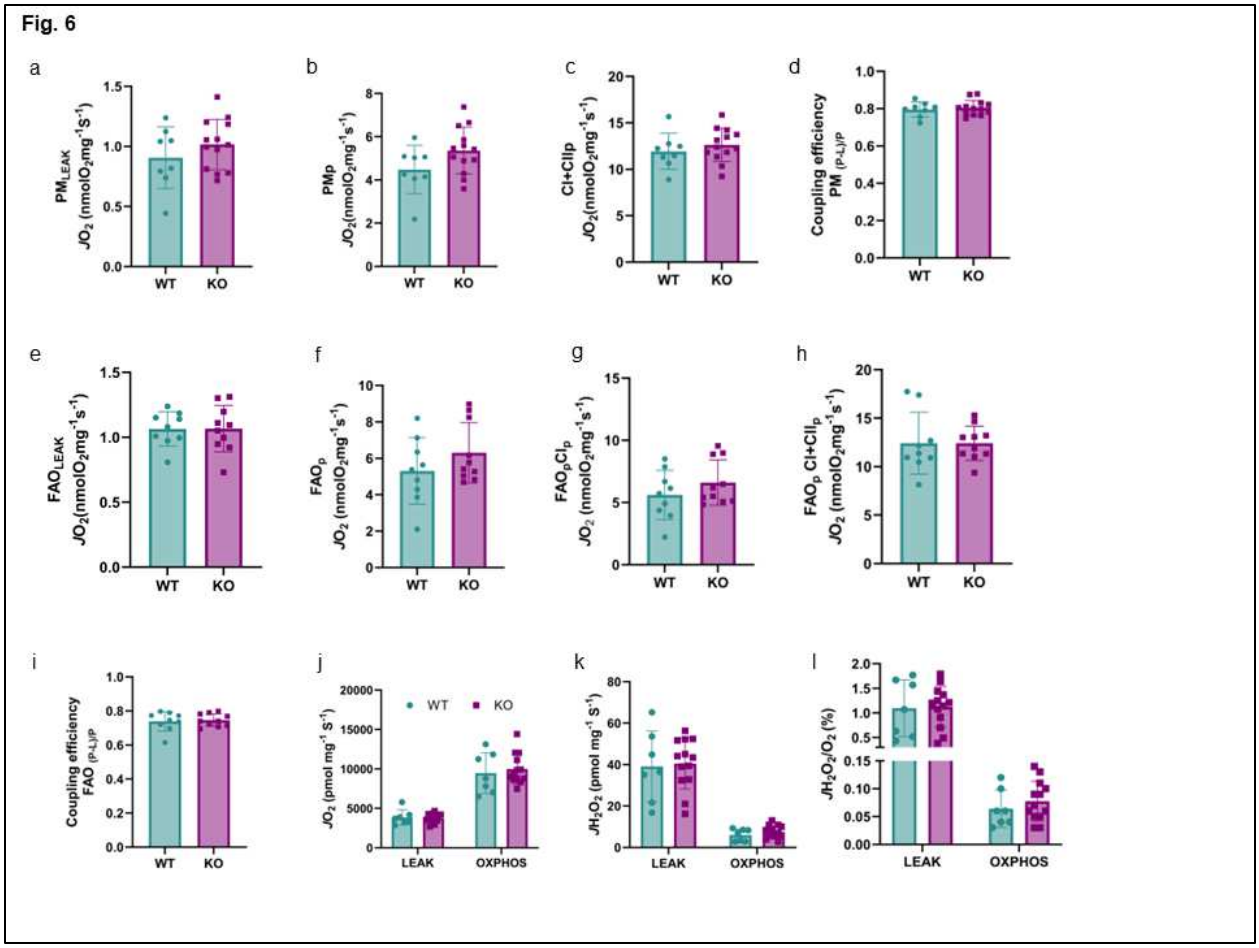

Coupling efficiency [(P − L)/P] was also similar (P = 0.6250; Fig. 6d). With octanoylcarnitine and malate (OctM) as substrates (n = 9 WT and 10 KO; Fig. 6E–H), fatty acid–supported LEAK respiration (FAO_{LEAK}; P = 0.9818) and OXPHOS (FAOp; P = 0.2311) did not differ between genotypes, nor did OXPHOS after the subsequent addition of pyruvate (FAOp CIp; P = 0.2693) and succinate (FAOp CI+CIIp; P = 0.9972; Fig. 6e–h). Fatty acid–linked coupling efficiency was also similar (P =0.751; Fig. 6i).

Mitochondrial H_2O_2 emission was measured together with O_2 consumption by O2k-fluorometry, with pyruvate and malate (n = 7 WT and 13 KO; Fig. 6j-l). O_2 flux (JO_2) did not differ between genotypes in the LEAK (P = 0.8092) or OXPHOS state (P = 0.6525; Fig. 6j). H_2O_2 emission (JH_2O_2) was also similar between genotypes in the LEAK (P = 0.8534) and OXPHOS states (P = 0.2780; Fig. 6k), as was H_2O_2 emission relative to O_2 flux (JH_2O_2/JO_2; LEAK, P =

0.9039; OXPHOS, P = 0.3535; Fig. 6l). These results show that endothelial *Shank3* deletion did not alter cardiac mitochondrial respiration or H_2O_2 emission under the conditions tested.

Lower Mitochondrial 4-HNE and Higher AMPK Phosphorylation in Endothelial Shank3-KO Hearts

To assess mitochondrial protein content and oxidative modification, Western blotting was performed on isolated cardiac mitochondria (Fig. 7a, b) and left-ventricular lysates (Fig. 7c, d). Protein levels of OXPHOS complexes I–V did not differ between groups (q = 0.6809, 0.5409, 0.1273, 0.4295, and 0.5409 for complexes I–V, respectively; Fig. 7a). The abundance of a 66-kDa 4-HNE-immunoreactive protein band was lower in mitochondrial preparations from KO than from WT mice (P = 0.0064; Fig. 7b).

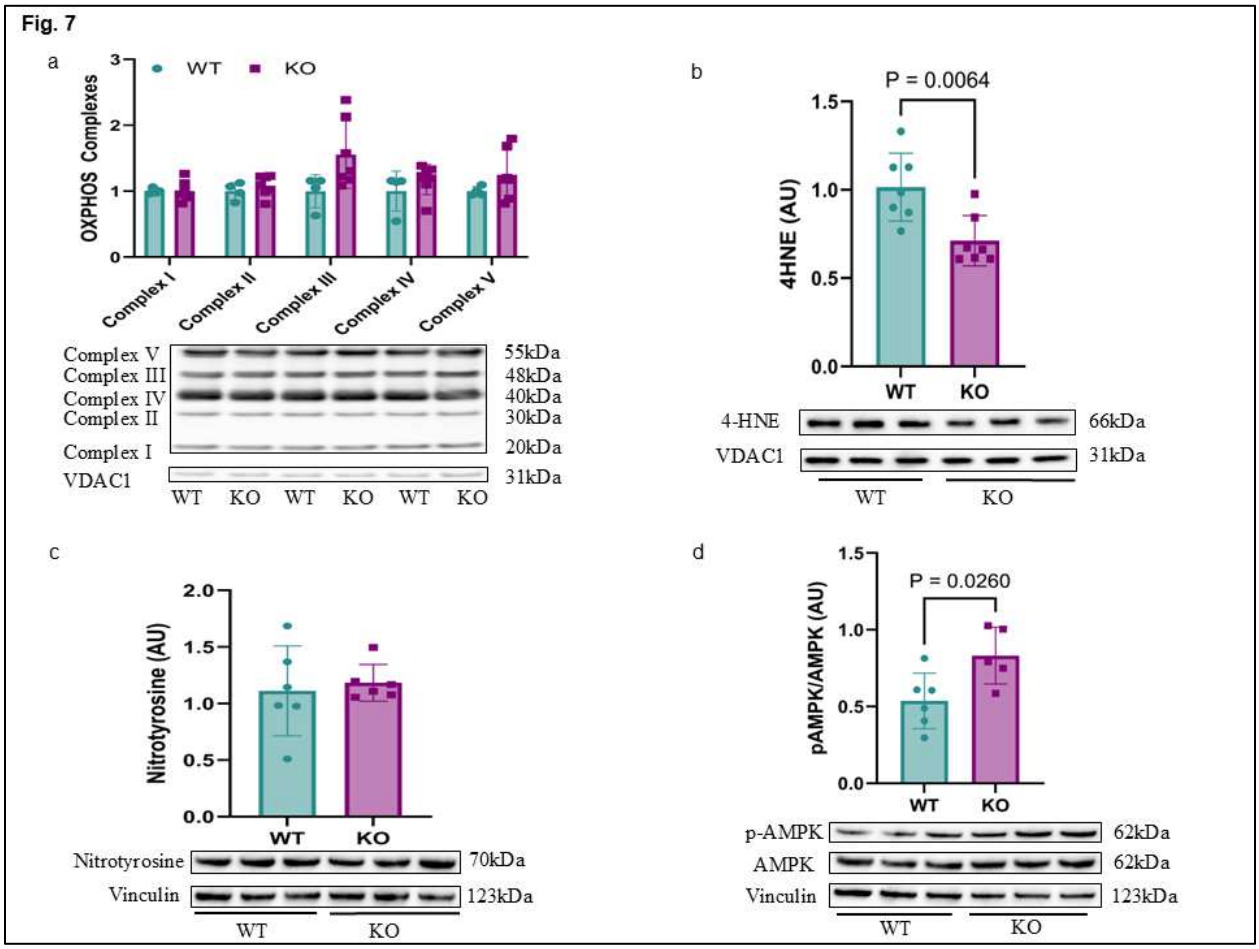

In LV lysates (Fig. 7c, d), the abundance of a 70-kDa nitrotyrosine-immunoreactive band did not differ between genotypes (P = 0.6958; Fig. 7c). Total AMPK protein abundance

normalized to vinculin was unchanged, whereas the ratio of phosphorylated AMPK (Thr172) to total AMPK was higher in KO than in WT mice (P = 0.0260; Fig. 7d).

Discussion

In this study, we examined overlapping subsets of adult male WT and eShank3-KO mice between 12 and 21 weeks of age. At 12–15 weeks, eShank3-KO mice exhibited greater IVRT shortening during β-adrenergic stimulation, whereas at 16 weeks, they had higher aortic peak velocity than WT mice. By 20–21 wk of age, KO mice had greater LV and atrial weights, LV dilation with normal wall thickness, and lower EF, FS, and posterior wall thickening, whereas SV and CO were maintained. This eccentric remodeling occurred without detectable myocardial fibrosis or induction of the measured fetal genes, and it was accompanied by lower *Myh6* and *Nppb* expressions. Mitochondrial respiratory capacity and H_2O_2 emission did not differ between genotypes, whereas mitochondrial 4-HNE was lower and the p-AMPK/AMPK ratio and *Ppargc1a* expression were higher in KO hearts. To our knowledge, these data are the first to show that *Shank3* deletion in Tek-Cre–targeted cells, which are mainly endothelial cells, is associated with eccentric LV remodeling and reduced systolic function in adult mice.

Previous studies of cardiac *Shank3* have focused mainly on cardiomyocytes. In cardiomyocytes, *Shank3* forms a complex with phospholipase Cβ1b at the sarcolemma and supports Gq-mediated hypertrophic signaling [15]. The effects of cardiomyocyte *Shank3* also appear to depend on its expression level. During natural aging, cardiac *Shank3* expression increases, and greater binding of *Shank3* to CaMKII limits Parkin-mediated mitophagy; cardiomyocyte-specific *Shank3* deletion reduced mitochondrial ROS production and preserved cardiac function in aged mice [43]. In contrast, transgenic mice carrying extra copies of the *Shank3* gene developed arrhythmias, sudden cardiac death, slower decay of cytosolic Ca^{2+} transients, and lower troponin I levels [22]. Our findings extend this work to the endothelium.

Together, these studies suggest that the cardiac effects of *Shank3* depend on both the cell type in which it is altered and its level of expression.

At 16 weeks of age, KO mice exhibited higher aortic peak velocity than WT mice. Because aortic velocity is influenced by stroke volume, aortic cross-sectional area, and afterload, this difference does not necessarily indicate greater intrinsic contractility. Although stroke volume did not differ significantly between genotypes at 20–21 weeks ($P = 0.1078$), it was not measured during the earlier Doppler assessment. Moreover, LV structure was not assessed at 16 weeks, and aortic flow was not reassessed at 20–21 weeks. Thus, the relationship between higher aortic velocity and eccentric LV remodeling remains unclear. Longitudinal assessment of LV structure, aortic dimensions, and blood pressure is needed to determine whether altered hemodynamic loading contributes to the remodeling phenotype.

During dobutamine stimulation, IVRT shortened in KO mice but not in WT mice, with a significant genotype × dobutamine interaction. Because IVRT is influenced by both LV relaxation and loading conditions, the underlying mechanism cannot be determined without direct measurement of LV filling pressures [35]. This finding should be interpreted cautiously because only five WT and eight KO mice met the heart rate response criterion following dobutamine administration. A-peak velocity was also modestly lower in KO mice across both conditions, potentially reflecting differences in atrial function or loading conditions.

By 20–21 wk of age, LV weight was approximately 20% greater in KO mice than in WT mice, and this was accompanied by larger LV diameters and volumes with normal wall thickness. This pattern indicates eccentric remodeling. Eccentric hypertrophy develops in response to volume overload, with increased diastolic wall stress serving as an important stimulus for ventricular remodeling [18]. EF, FS, and posterior wall thickening were lower in KO mice, but the reduction in EF was modest (71% vs. 60%), and SV and CO were maintained. Ventricular dysfunction alone is insufficient to establish heart failure in animal models; additional

evidence consistent with the syndrome, such as congestion, elevated filling pressures, impaired exercise capacity, or impaired perfusion associated with reduced cardiac output, should be demonstrated [34]. We did not measure these indices. We therefore describe this phenotype as eccentric remodeling with mildly reduced systolic function rather than heart failure. Atrial weight was also greater in KO mice. Although left atrial enlargement is associated with LV diastolic dysfunction [40], increased atrial weight alone does not establish elevated LV filling pressure and may also reflect primary atrial remodeling. Doppler mitral inflow indices obtained in this study provide only an indirect assessment of diastolic function and cannot estimate LV filling pressure reliably in mice [35]. Invasive measurement of LV end-diastolic pressure, together with lung weight and systemic blood pressure, will be needed to characterize the hemodynamic phenotype and clarify the mechanisms of remodeling in this model.

The molecular profile of knockout hearts differed from that of most models of pathological remodeling. Pathological remodeling is usually accompanied by interstitial fibrosis and re-expression of fetal genes such as *Nppa*, *Nppb*, *Acta1*, and *Myh7* [17]. Collagen area and the expression of the measured fibrosis-related genes did not differ between genotypes. With only three hearts per genotype, this analysis cannot exclude a small fibrotic change. *Nppa*, *Acta1*, and *Myh7* were unchanged, and *Atp2a2*, which encodes SERCA2a, was also unchanged. *Nppb* was lower rather than increased. Lack of fibrosis and fetal-gene induction can occur in physiological hypertrophy [4]. The lower ejection fraction and fractional shortening indicate that the remodeling was not an uncomplicated physiological response, but these functional changes alone do not establish a pathological gene program. Knockout hearts instead showed lower *Myh6* expression. *Myh6* encodes α-myosin heavy chain (α-MHC), the predominant and faster myosin heavy-chain isoform in the adult mouse ventricle. A lower α-MHC content could slow cross-bridge cycling and contribute to the lower fractional shortening.

Because myosin heavy-chain protein isoforms were not measured, this possibility remains to be tested.

The lower *Nppb* expression was unexpected. In heart failure, reduced forward output activates neurohormonal systems that promote renal sodium and water retention [36]. The resulting volume overload stretches the ventricle and increases *Nppb* expression. Knockout mice had a lower body weight and a lower free body fluid (FBF) content relative to body weight. If this reflected a smaller body fluid volume, it might help explain why *Nppb* was not increased, but it would not explain why *Nppb* was lower than in wild-type hearts. It is also difficult to reconcile with the eccentric remodeling described above. This interpretation has important limitations. FBF measured by time-domain NMR (Bruker minispec) is the proton signal from water that is not bound within lean tissue or fat. That signal may include extracellular fluid and fluid in the bladder and gastrointestinal tract, and it is not a validated measure of plasma or interstitial volume. Only FBF normalized to body weight differed between groups; absolute FBF did not. Plasma volume, circulating natriuretic peptides, and tissue water content were not measured. The lower *Nppb* expression therefore cannot be attributed to reduced body fluid, and its cause remains unclear.

The mechanisms underlying cardiac remodeling in eShank3-KO mice remain unclear. Kim et al. demonstrated that endothelial *Shank3* deletion disrupted tight-junction proteins and increased blood–brain barrier permeability in neonatal male mice, although permeability normalized in adulthood [20]. Whether similar alterations occur in the cardiac microvasculature is unknown. Endothelial cells also regulate myocardial growth and contractility through paracrine signaling [5], and disruption of VEGF- or neuregulin-dependent signaling can cause cardiac dysfunction [13,7]. Notably, PGC-1α, best known for regulating mitochondrial metabolism, also promotes cardiac angiogenesis through VEGF signaling [26]. Among the angiogenesis-related genes examined, only *Ppargc1a* expression was significantly higher in KO hearts, whereas

Vegfa, *Angpt1*, *Angpt2*, *Pdgfa*, and *Fgf2* were unchanged. Because capillary density and VEGF protein abundance were not assessed, the functional significance of *Ppargc1a* upregulation for cardiac angiogenesis remains unclear.

Interestingly, global *Shank3* Δexon 4–9 mutant mice exhibited only subtle LV structural abnormalities [2]. This difference may reflect cell-type-specific effects of *Shank3* deletion, although differences in age, experimental methods, and control groups may also contribute. Future studies examining cardiac microvascular structure and permeability, blood pressure, and endothelial–cardiomyocyte signaling are needed to clarify the mechanisms underlying the observed remodeling.

Despite LV dilation and reduced EF, mitochondrial respiration supported by carbohydrate- and fatty acid-derived substrates, coupling efficiency, and H_2O_2 emission did not differ between genotypes. Because these measurements were performed in isolated mitochondria and normalized to mitochondrial protein, they reflect intrinsic respiratory capacity under the conditions tested rather than total mitochondrial content or myocardial energy status *in vivo*. Interestingly, KO hearts exhibited a higher p-AMPK/AMPK ratio, which may indicate altered myocardial energy sensing, although energy status was not directly assessed [44]. *Ppargc1a* expression was also higher in KO hearts. Beyond its role in angiogenesis, PGC-1α contributes to cardiac adaptation to pressure overload and mitochondrial antioxidant defenses [1,24]. Thus, increased *Ppargc1a* expression may represent an adaptive response. Although we attempted to assess PGC-1α protein abundance by Western blotting, nonspecific immunoreactive bands prevented reliable quantification, consistent with previously reported limitations in PGC-1α antibody specificity [12]. Therefore, whether increased *Ppargc1a* mRNA expression translates into greater PGC-1α protein abundance or enhanced downstream antioxidant defenses remains unknown. The relative abundance of OXPHOS complex subunits was unchanged, whereas immunoreactivity of a 66-kDa mitochondrial 4-HNE-modified protein

band was lower in KO hearts. In contrast, the 70-kDa nitrotyrosine-immunoreactive band in LV lysates did not differ between genotypes. These findings do not establish a generalized reduction in oxidative stress, and the relationship between AMPK/PGC-1α signaling and lower mitochondrial 4-HNE immunoreactivity remains to be determined.

Although the underlying mechanisms remain unclear, our findings may have clinical relevance to SHANK3-related disorders. In a recent case series, all five patients with pathogenic *SHANK3* variants exhibited cardiac abnormalities, including mild or borderline ventricular dysfunction in three patients [10]. Our findings raise the possibility that SHANK3 dysfunction in endothelial cells contributes to cardiac abnormalities in these disorders, although this potential mechanism requires further investigation.

This study has several limitations. First, WT controls were age-matched C57BL/6J mice obtained from The Jackson Laboratory rather than littermates, and Tek-Cre-only and floxed-only controls were not available. Therefore, potential confounding effects of the Cre transgene, genetic background, and rearing environment cannot be excluded. Second, although this model was previously characterized for endothelial *Shank3* deletion [20], Tek-Cre–mediated recombination is not restricted to vascular endothelial cells and can also involve hematopoietic and endocardial-derived lineages [38,27]. Consequently, contributions from these additional cell populations to the cardiac phenotype cannot be excluded. We did not confirm *Shank3* loss in cardiac endothelial cells in this cohort, so the phenotype cannot be attributed exclusively to endothelial cells. Third, we did not measure blood pressure, LV pressures, lung weight, plasma volume, or circulating natriuretic peptides. These measures are needed to determine whether KO mice develop heart failure and to clarify their volume status. Fourth, dobutamine was given as a single i.p. injection rather than as a continuous intravenous infusion. Under these conditions, heart rate increased only modestly (by approximately 10–15%), and not all mice met the response criterion. Our protocol may therefore have underestimated β-adrenergic reserve,

and a graded infusion protocol would allow a more complete assessment of contractile and lusitropic reserve. Fifth, we did not measure cardiomyocyte size or capillary density, which would help to define the type of hypertrophy and the role of the microvasculature. Sixth, myocardial transcript profiling was restricted to a targeted panel of 17 genes chosen a priori and measured in whole left ventricle, so pathways outside this panel and the cell populations driving the observed differences cannot be resolved. Finally, only male mice were studied. We studied males because ASD is 3.4 times more prevalent in boys than in girls [37] and because Kim et al. consistently observed male-predominant phenotypes in eShank3-KO mice, including abnormal tight-junction structure, increased neonatal BBB permeability, impaired neuronal excitability, and autistic-like behaviors [20]. Because sex can modify cardiac remodeling [39], future studies should determine whether female eShank3-KO mice develop a similar cardiac phenotype. The long-term consequences of this remodeling, including survival and susceptibility to arrhythmias at older ages (e.g., >12 months), also remain to be determined.

In conclusion, *Shank3* deletion in Tek-Cre–targeted cells, which are mainly endothelial cells, was associated with eccentric LV remodeling and mildly reduced systolic function in adult male mice. This remodeling occurred without detectable fibrosis, fetal gene induction, or loss of mitochondrial respiratory capacity, and it was accompanied by lower mitochondrial 4-HNE immunoreactivity at approximately 66 kDa, higher AMPK phosphorylation, and higher *Ppargc1a* expression. These findings suggest that endothelial *Shank3* contributes to the maintenance of normal cardiac structure and function, and they identify the endothelium as a potential link between *SHANK3* deficiency and cardiac abnormalities.

Data availability

Raw datasets are available from the corresponding author (Eunhee Chung, eunhee.chung@utsa.edu) upon reasonable request.

Supplementary information

Genotyping primer sequences are provided in Supplementary Table 1.

Declarations

Ethics approval: All procedures were approved by the Institutional Animal Care and Use Committee of the University of Texas at San Antonio (Protocol Nos. MU104 and MU109) and were conducted in accordance with the U.S. National Research Council's Guide for the Care and Use of Laboratory Animals (8th edition, 2011) and is reported according to the ARRIVE 2.0 guidelines [28]. No human participants were involved.

Competing interests

No conflicts of interest, financial or otherwise, are declared by the authors.

Author contributions

E.C., S.C.L., and I.H.K. conceived the research. E.C. designed the study. S.C.L. and I.H.K. provided the mice. C.C. performed genotyping of all mice. Y.-J.F., A.O., and A.G performed the experiments. E.C., Y.-J.F., and A.G. prepared the figures. E.C. drafted the manuscript. All authors critically reviewed, edited, and revised the manuscript and approved the final version.

Funding

This work was supported by the University of Texas at San Antonio Lutcher Brown Fellowship (E.C.); the Mindfull Foundation (C.C.); the UTSA Neuroscience Pilot Program (S.C.L.); start-up funds from Texas Tech University Health Sciences Center (S.C.L.); and National Institutes of Health grants R01MH117429 and R01AG075000 (I.H.K.).

Acknowledgements

The authors acknowledge Kassandra Gonzalez, U-Ter Aondo Jia, Fernando Sosa, Catherine De Guzman, and Siril Vajja for their assistance with this study. The graphical abstract was created using BioRender.com. The BioRender publication license has been submitted as a separate file.

References

1. Arany Z, Novikov M, Chin S, Ma Y, Rosenzweig A, Spiegelman BM (2006) Transverse aortic constriction leads to accelerated heart failure in mice lacking PPAR-gamma coactivator 1alpha. Proc Natl Acad Sci U S A 103:10086–10091. doi:10.1073/pnas.0603615103
2. Assimopoulos S, Hammill C, Fernandes DJ, Spencer Noakes TL, Zhou YQ, Nutter LMJ, Ellegood J, Anagnostou E, Sled JG, Lerch JP (2022) Genetic mouse models of autism spectrum disorder present subtle heterogenous cardiac abnormalities. Autism Res 15:1189–1208. doi:10.1002/aur.2728
3. Benjamini Y, Krieger AM, Yekutieli D (2006) Adaptive linear step-up procedures that control the false discovery rate. Biometrika 93:491–507. doi:DOI 10.1093/biomet/93.3.491
4. Bernardo BC, Weeks KL, Pretorius L, McMullen JR (2010) Molecular distinction between physiological and pathological cardiac hypertrophy: experimental findings and therapeutic strategies. Pharmacology & Therapeutics 128:191–227. doi:10.1016/j.pharmthera.2010.04.005
5. Brutsaert DL (2003) Cardiac endothelial-myocardial signaling: its role in cardiac growth, contractile performance, and rhythmicity. Phys Rev 83:59–115. doi:10.1152/physrev.00017.2002
6. Chung E, Yeung F, Leinwand LA (2013) Calcineurin activity is required for cardiac remodelling in pregnancy. Cardiovascular Research 100:402–410. doi:10.1093/cvr/cvt208
7. Crone SA, Zhao YY, Fan L, Gu Y, Minamisawa S, Liu Y, Peterson KL, Chen J, Kahn R, Condorelli G, Ross J, Jr., Chien KR, Lee KF (2002) ErbB2 is essential in the prevention of dilated cardiomyopathy. Nat Med 8:459–465. doi:10.1038/nm0502-459
8. Dirkx E, da Costa Martins PA, De Windt LJ (2013) Regulation of fetal gene expression in heart failure. Biochimica et Biophysica Acta 1832:2414–2424. doi:10.1016/j.bbadis.2013.07.023
9. Eisner DA (2021) Pseudoreplication in physiology: More means less. J Gen Physiol 153. doi:10.1085/jgp.202012826
10. Esmel-Vilomara R, Dougherty-De Miguel L, Artigas-Baleri A, Turon-Vinas E, Cusco I, Diaz-Gomez A, Panades-De Oliveira L, Rocamora R, Boronat S (2024) Cardiovascular abnormalities in patients with SHANK3 pathogenic variants: Beyond neurodevelopmental disorders and epilepsy. Eur J Med Genet 71:104965. doi:10.1016/j.ejmg.2024.104965
11. Fang YJ, Gonzalez K, Konecny F, Chicco AJ, Chung E (2026) Maternal exercise is associated with enhanced systolic reserve and altered mitochondrial respiration in adult female offspring. Am J Physiol Heart Circ Physiol 331:H423–H439. doi:10.1152/ajpheart.00277.2026
12. Galipeau M, Schmitt C, Baldwin C, Gunes A, Estall JL (2024) Commercially available PGC-1alpha antibodies vary greatly in specificity and sensitivity. MicroPubl Biol 2024. doi:10.17912/micropub.biology.001268
13. Giordano FJ, Gerber HP, Williams SP, VanBruggen N, Bunting S, Ruiz-Lozano P, Gu Y, Nath AK, Huang Y, Hickey R, Dalton N, Peterson KL, Ross J, Jr., Chien KR, Ferrara N (2001) A cardiac myocyte vascular endothelial growth factor paracrine pathway is required to maintain cardiac function. Proc Natl Acad Sci U S A 98:5780–5785. doi:10.1073/pnas.091415198
14. Gonzalez K, Merlin AC, Roye E, Ju B, Lee Y, Chicco AJ, Chung E (2024) Voluntary Wheel Running Reduces Cardiometabolic Risks in Female Offspring Exposed to Lifelong High-Fat, High-Sucrose Diet. Med Sci Sports Exerc 56:1378–1389. doi:10.1249/MSS.0000000000003443

15. Grubb DR, Iliades P, Cooley N, Yu YL, Luo J, Filtz TM, Woodcock EA (2011) Phospholipase Cbeta1b associates with a Shank3 complex at the cardiac sarcolemma. FASEB J 25:1040–1047. doi:10.1096/fj.10-171470
16. Halldorsdottir S, Carmody J, Boozer CN, Leduc CA, Leibel RL (2009) Reproducibility and accuracy of body composition assessments in mice by dual energy x-ray absorptiometry and time domain nuclear magnetic resonance. Int J Body Compos Res 7:147–154
17. Heineke J, Molkentin JD (2006) Regulation of cardiac hypertrophy by intracellular signalling pathways. Nature Reviews Molecular Cell Biology 7:589–600. doi:10.1038/nrm1983
18. Ikeda M, Ide T, Fujino T, Matsuo Y, Arai S, Saku K, Kakino T, Oga Y, Nishizaki A, Sunagawa K (2015) The Akt-mTOR axis is a pivotal regulator of eccentric hypertrophy during volume overload. Sci Rep 5:15881. doi:10.1038/srep15881
19. Kim Y, Ko TH, Jin C, Zhang Y, Kang HR, Ma R, Li H, Choi JI, Han K (2023) The emerging roles of Shank3 in cardiac function and dysfunction. Front Cell Dev Biol 11:1191369. doi:10.3389/fcell.2023.1191369
20. Kim YE, Kim M, Kim S, Lee R, Ujihara Y, Marquez-Wilkins EM, Jiang YH, Yang E, Kim H, Lee C, Park C, Kim IH (2025) Endothelial SHANK3 regulates tight junctions in the neonatal mouse blood-brain barrier through beta-Catenin signaling. Nat Commun 16:1407. doi:10.1038/s41467-025-56720-1
21. Kisanuki YY, Hammer RE, Miyazaki J, Williams SC, Richardson JA, Yanagisawa M (2001) Tie2-Cre transgenic mice: a new model for endothelial cell-lineage analysis in vivo. Developmental Biology 230:230–242. doi:10.1006/dbio.2000.0106
22. Ko TH, Kim Y, Jin C, Yu B, Lee M, Luong PK, Trinh TN, Yang Y, Kang H, Zhang Y, Ma R, Yoo K, Choi J, Kim JY, Woo SH, Han K, Choi JI (2025) Shank3 Overexpression Leads to Cardiac Dysfunction in Mice by Disrupting Calcium Homeostasis in Cardiomyocytes. Korean Circ J 55:100–117. doi:10.4070/kcj.2024.0179
23. Li Puma LC, Hedges M, Heckman JM, Mathias AB, Engstrom MR, Brown AB, Chicco AJ (2020) Experimental oxygen concentration influences rates of mitochondrial hydrogen peroxide release from cardiac and skeletal muscle preparations. Am J Physiol Regul Integr Comp Physiol 318:R972–R980. doi:10.1152/ajpregu.00227.2019
24. Lu Z, Xu X, Hu X, Fassett J, Zhu G, Tao Y, Li J, Huang Y, Zhang P, Zhao B, Chen Y (2010) PGC-1 alpha regulates expression of myocardial mitochondrial antioxidants and myocardial oxidative stress after chronic systolic overload. Antioxid Redox Signal 13:1011–1022. doi:10.1089/ars.2009.2940
25. Man W, Gu J, Wang B, Zhang M, Hu J, Lin J, Sun D, Xiong Z, Gu X, Hao K, Guo B, Wei G, Zhang L, Song R, Li C, Wang H, Sun D (2020) SHANK3 Co-ordinately Regulates Autophagy and Apoptosis in Myocardial Infarction. Front Physiol 11:1082. doi:10.3389/fphys.2020.01082
26. Patten IS, Rana S, Shahul S, Rowe GC, Jang C, Liu L, Hacker MR, Rhee JS, Mitchell J, Mahmood F, Hess P, Farrell C, Koulisis N, Khankin EV, Burke SD, Tudorache I, Bauersachs J, del Monte F, Hilfiker-Kleiner D, Karumanchi SA, Arany Z (2012) Cardiac angiogenic imbalance leads to peripartum cardiomyopathy. Nature 485:333–338. doi:10.1038/nature11040
27. Payne S, De Val S, Neal A (2018) Endothelial-specific Cre mouse models: Is your Cre CREdibile? Arteriosclerosis, Thrombosis, and Vascular Biology 38:2550–2561
28. Percie du Sert N, Hurst V, Ahluwalia A, Alam S, Avey MT, Baker M, Browne WJ, Clark A, Cuthill IC, Dirnagl U, Emerson M, Garner P, Holgate ST, Howells DW, Karp NA, Lazic SE, Lidster K, MacCallum CJ, Macleod M, Pearl EJ, Petersen OH, Rawle F, Reynolds P, Rooney K, Sena ES, Silberberg SD, Steckler T, Wurbel H (2020) The ARRIVE guidelines 2.0: Updated guidelines for reporting animal research. PLoS Biol 18:e3000410. doi:10.1371/journal.pbio.3000410

667 29. Perez JET, Ortiz-Urbina J, Heredia CP, Pham TT, Madala S, Hartley CJ, Entman ML, Taffet
668 GE, Reddy AK (2021) Aortic acceleration as a noninvasive index of left ventricular
669 contractility in the mouse. Sci Rep 11:536. doi:10.1038/s41598-020-79866-y
670 30. Pinto AR, Ilinykh A, Ivey MJ, Kuwabara JT, D'Antoni ML, Debuque R, Chandran A, Wang L,
671 Arora K, Rosenthal NA, Tallquist MD (2016) Revisiting Cardiac Cellular Composition.
672 Circ Res 118:400–409. doi:10.1161/CIRCRESAHA.115.307778
673 31. Reddy AK, Taffet GE, Li YH, Lim SW, Pham TT, Pocius JS, Entman ML, Michael LH,
674 Hartley CJ (2005) Pulsed Doppler signal processing for use in mice: applications. IEEE
675 Trans Biomed Eng 52:1771–1783. doi:10.1109/TBME.2005.855709
676 32. Remes A, Noormalal M, Schmiedel N, Frey N, Frank D, Muller OJ, Graf M (2023) Adapted
677 clustering method for generic analysis of histological fibrosis staining as an open source
678 tool. Sci Rep 13:4389. doi:10.1038/s41598-023-30196-9
679 33. Ricciardello A, Tomaiuolo P, Persico AM (2021) Genotype-phenotype correlation in Phelan-
680 McDermid syndrome: A comprehensive review of chromosome 22q13 deleted genes.
681 Am J Med Genet A 185:2211–2233. doi:10.1002/ajmg.a.62222
682 34. Roh J, Hill JA, Singh A, Valero-Munoz M, Sam F (2022) Heart Failure With Preserved
683 Ejection Fraction: Heterogeneous Syndrome, Diverse Preclinical Models. Circ Res
684 130:1906–1925. doi:10.1161/CIRCRESAHA.122.320257
685 35. Schnelle M, Catibog N, Zhang M, Nabeebaccus AA, Anderson G, Richards DA, Sawyer G,
686 Zhang X, Toischer K, Hasenfuss G, Monaghan MJ, Shah AM (2018) Echocardiographic
687 evaluation of diastolic function in mouse models of heart disease. J Mol Cell Cardiol
688 114:20–28. doi:10.1016/j.yjmcc.2017.10.006
689 36. Schrier RW, Abraham WT (1999) Hormones and hemodynamics in heart failure. New
690 England Journal of Medicine 341:577–585. doi:10.1056/NEJM199908193410806
691 37. Shaw KA, Williams S, Patrick ME, Valencia-Prado M, Durkin MS, Howerton EM, Ladd-
692 Acosta CM, Pas ET, Bakian AV, Bartholomew P, Nieves-Munoz N, Sidwell K, Alford A,
693 Bilder DA, DiRienzo M, Fitzgerald RT, Furnier SM, Hudson AE, Pokoski OM, Shea L,
694 Tinker SC, Warren Z, Zahorodny W, Agosto-Rosa H, Anbar J, Chavez KY, Esler A,
695 Forkner A, Grzybowski A, Agib AH, Hallas L, Lopez M, Magana S, Nguyen RHN, Parker
696 J, Pierce K, Protho T, Torres H, Vanegas SB, Vehorn A, Zhang M, Andrews J, Greer F,
697 Hall-Lande J, McArthur D, Mitamura M, Montes AJ, Pettygrove S, Shenouda J, Skowyra
698 C, Washington A, Maenner MJ (2025) Prevalence and Early Identification of Autism
699 Spectrum Disorder Among Children Aged 4 and 8 Years - Autism and Developmental
700 Disabilities Monitoring Network, 16 Sites, United States, 2022. MMWR Surveill Summ
701 74:1–22. doi:10.15585/mmwr.ss7402a1
702 38. Tang Y, Harrington A, Yang X, Friesel RE, Liaw L (2010) The contribution of the Tie2+
703 lineage to primitive and definitive hematopoietic cells. Genesis 48:563–567.
704 doi:10.1002/dvg.20654
705 39. Tripathi R, Sullivan R, Fan TM, Wang D, Sun Y, Reed GL, Gladysheva IP (2017) Enhanced
706 heart failure, mortality and renin activation in female mice with experimental dilated
707 cardiomyopathy. PLoS ONE 12:e0189315. doi:10.1371/journal.pone.0189315
708 40. Tsang TS, Barnes ME, Gersh BJ, Bailey KR, Seward JB (2002) Left atrial volume as a
709 morphophysiologic expression of left ventricular diastolic dysfunction and relation to
710 cardiovascular risk burden. Am J Cardiol 90:1284–1289. doi:10.1016/s0002-
711 9149(02)02864-3
712 41. Uchino S, Waga C (2013) SHANK3 as an autism spectrum disorder-associated gene. Brain
713 Dev 35:106–110. doi:10.1016/j.braindev.2012.05.013
714 42. Wang X, McCoy PA, Rodriguiz RM, Pan Y, Je HS, Roberts AC, Kim CJ, Berrios J, Colvin
715 JS, Bousquet-Moore D, Lorenzo I, Wu G, Weinberg RJ, Ehlers MD, Philpot BD, Beaudet
716 AL, Wetsel WC, Jiang YH (2011) Synaptic dysfunction and abnormal behaviors in mice

lacking major isoforms of *Shank3*. Hum Mol Genet 20:3093–3108. doi:10.1093/hmg/ddr212
43. Wang Y, Xu Y, Guo W, Fang Y, Hu L, Wang R, Zhao R, Guo D, Qi B, Ren G, Ren J, Li Y, Zhang M (2022) Ablation of Shank3 alleviates cardiac dysfunction in aging mice by promoting CaMKII activation and Parkin-mediated mitophagy. Redox Biol 58:102537. doi:10.1016/j.redox.2022.102537
44. Zaha VG, Young LH (2012) AMP-activated protein kinase regulation and biological actions in the heart. Circ Res 111:800–814. doi:10.1161/CIRCRESAHA.111.255505
45. Zhou B, Tian R (2018) Mitochondrial dysfunction in pathophysiology of heart failure. Journal of Clinical Investigation 128:3716–3726. doi:10.1172/JCI120849

FIGURE LEGENDS

Fig. 1 Body weight, body composition, and cardiac morphometry in endothelial Shank3-knockout mice. Measurements in 20- to 21-week-old male wild-type (WT) and endothelial Shank3-knockout (KO) mice. **a,** total body weight (BW). **b and c,** body composition: absolute fat mass, lean mass, and free body fluid (FBF) mass (b), and the same measures expressed as a percentage of BW (c). **d–f**, left ventricular morphometry: absolute left ventricular weight (LVW; d), LVW normalized to BW (LVW/BW; e), and LVW normalized to tibia length (LVW/TL; f). **g–i**, atrial morphometry: absolute atrial weight (AW; g), AW normalized to BW (AW/BW; h), and AW normalized to TL (AW/TL; i). Bars show means ± SD, and each symbol represents one mouse (a and d–i: WT, n = 16–18; KO, n = 14–16. B and C: WT, n = 11; KO, n = 10). WT and KO mice were compared with unpaired, two-tailed Welch's t tests in **a** and **d–i**. Body composition variables (**b and c**) were compared with multiple Mann–Whitney tests, with the false discovery rate controlled at 5%; the number above the bracket in **c** is a q value.

Fig. 2 Mitral inflow and isovolumic time intervals at baseline and during β-adrenergic stimulation.

Pulsed-wave Doppler measurements of mitral inflow at baseline and during dobutamine stimulation in 12-to-15 week-old male wild-type (WT) and endothelial Shank3-knockout (KO) mice. Heart rate (a), E-peak velocity (early filling; b), A-peak velocity (late, atrial filling; c), E/A

peak velocity ratio (d), isovolumic contraction time (IVCT; e), and isovolumic relaxation time (IVRT; f). Data are mean ± SD, and each symbol represents one mouse. Baseline: n = 16 WT and 16 KO mice. Dobutamine: n = 5 WT and 8 KO mice. Data were analyzed with a two-way mixed-effects model (genotype × condition), followed by Fisher's LSD multiple comparisons test. Numbers above brackets are P values from post hoc comparisons. P values for main effects and interactions are reported in the text.

Fig. 3 Aortic outflow at baseline and during β-adrenergic stimulation.

Pulsed-wave Doppler measurements of aortic outflow at baseline and during dobutamine stimulation in 16-week-old male wild-type (WT) and endothelial Shank3-knockout (KO) mice. Heart rate (a), aortic peak velocity (b), mean acceleration (c), and ejection time (d). Data are mean ± SD, and each symbol represents one mouse (n = 12 WT and 16 KO mice). Data were analyzed with a two-way mixed-effects model (genotype × condition), followed by Fisher's LSD multiple comparisons test. Numbers above brackets are P values from post hoc comparisons.

Fig. 4 Echocardiographic assessment of left ventricular structure and systolic function at 20–21 weeks.

M-mode echocardiography in the parasternal short-axis view at the mid-papillary level in 20- to 21-week-old wild-type (WT) and endothelial Shank3-knockout (KO) mice. **a,** heart rate (HR; a). **b–e**, LV wall thickness: anterior wall in diastole (LVAWd; b) and systole (LVAWs; c), and posterior wall in diastole (LVPWd; d) and systole (LVPWs; e). **f and g**, LV internal diameter in diastole (LVIDd; f) and systole (LVIDs; g). **h–k**, LV volumes and output: end-diastolic volume (EDV; h), end-systolic volume (ESV; i), stroke volume (SV; j), and cardiac output (CO; k). **l–o**, indices of systolic function: ejection fraction (%EF; l), fractional shortening (%FS; m), posterior wall thickening (%PWT; n), and anterior wall thickening (%AWT; o). LV volumes were calculated from LV internal diameters using the Teichholz formula. Data are mean ± SD, and each symbol

represents one mouse (n = 15 WT and 15 KO male mice). Groups were compared with Welch's t test. Numbers above brackets are P values.

Fig. 5 Myocardial fibrosis and cardiac transcriptional profiling.

a, Representative Masson's trichrome-stained heart sections from wild-type (WT) and endothelial Shank3-knockout (KO) mice at 4x (top row, scale bar, 500 μm; a) at 20x (bottom row, scale bar, 100 μm). **b,** Quantification of myocardial fibrosis, expressed as collagen-positive area relative to total myocardial tissue area (%), including perivascular regions. Three sections per mouse were analyzed, with the entire myocardial cross-sectional area imaged at 20× magnification (16–27 fields per section). Section-level percentages were averaged to obtain one value per mouse (n = 3 per genotype). Bars represent means ± SD, and each symbol represents one mouse. Groups were compared using Welch's t test. **c-e**, relative mRNA expression of genes associated with fibrosis (*Col1a1*, *Col3a1*, *Col8a1*, *Mmp3*, and *Ctgf*; c), hypertrophy and heart failure (*Nppa*, *Nppb*, *Acta1*, *Atp2a2*, *Myh7*, and *Myh6*; d), and angiogenesis-related genes (*Angpt1*, *Angpt2*, *Pdgfa*, *Vegfa*, *Fgf2*, and *Ppargc1a*; e). mRNA levels were normalized to 36B4 and are expressed relative to the WT mean. Data are mean ± SD, and each symbol represents one mouse (n = 6 per genotype). WT and KO mice were compared with multiple Mann–Whitney tests, with the false discovery rate controlled at 5% within each gene group. Numbers above brackets are q values.

Fig. 6 Cardiac mitochondrial respiration and H_2O_2 emission.

Mitochondria were isolated from the left ventricle of 20- to 21-week-old male wild-type (WT) and endothelial Shank3-knockout (KO) mice. **a–d**, pyruvate- and malate-supported respiration: LEAK respiration (PM_{LEAK}; a), ADP-stimulated OXPHOS (PMp; b), maximal OXPHOS after the addition of glutamate and succinate (CI+CIIp; c), and coupling efficiency [(P − L)/P; d]. e–i, fatty acid–supported respiration with octanoylcarnitine and malate: LEAK respiration (FAO_{LEAK}; e),

794 ADP-stimulated OXPHOS (FAOp; f), OXPHOS after the addition of pyruvate (FAOp CIp; g) and
795 succinate (FAOp CI+CIIp; h), and coupling efficiency [(P − L)/P; i]. j–l, O_2 flux (JO_2; j), H_2O_2
796 emission (JH_2O_2; k), and JH_2O_2/JO_2 (l) in the LEAK and OXPHOS states. Note the broken y-axis
797 in **l**. Rates are normalized to protein content (mitochondria). Data are mean ± SD, and each
798 symbol represents one mouse (respirometry: n = 8 WT and 13 KO for CHO; n=9 WT, 10 KO for
799 FAO; fluorometry: n = 7 WT and 13 KO). WT and KO mice were compared using Welch's t tests
800 for each respiratory parameter (**a–i**) and separately for each respiratory state (**j–l**).

801 **Fig. 7** Mitochondrial protein content, oxidative modification, and AMPK phosphorylation in the
802 heart.

803 **a and b**, Isolated cardiac mitochondria from male wild-type (WT) and endothelial Shank3-
804 knockout (KO) mice. **a,** OXPHOS complex subunits NDUFB8, SDHB, UQCRC2, MTCO1, and
805 ATP5A, normalized to VDAC1 (a). 4-HNE immunoreactivity at approximately 66 kDa,
806 normalized to VDAC1 (b). **c and d**, Left ventricular lysates. Nitrotyrosine immunoreactivity at
807 approximately 70 kDa, normalized to vinculin (c). Phosphorylated AMPK (Thr172) relative to
808 total AMPK; vinculin is shown as the lysate loading control (d). Representative blots are shown
809 below each graph. Values were normalized to the mean of WT samples on the same blot.
810 Samples were analyzed on 2–3 blots, and repeated measurements were averaged to obtain
811 one value per mouse. Data are means ± SD, with each symbol representing one mouse (n = 4–
812 6 WT and 5–7 KO). OXPHOS complex subunits (a) were compared using multiple Mann–
813 Whitney tests, with the false discovery rate controlled at 5% across the five subunits.
814 Comparisons in **b–d** were performed using Welch's t tests. Numbers above brackets indicate P
815 values; q values for OXPHOS complexes I–V are reported in the Results.